Geometry and Mechanics in the Opening of Chiral Seed Pods
Shahaf Armon, *et al.*
Science **333**, 1726 (2011);
DOI: 10.1126/science.1203874

This copy is for your personal, non-commercial use only.

If you wish to distribute this article to others, you can order high-quality copies for your colleagues, clients, or customers by clicking here.

Permission to republish or repurpose articles or portions of articles can be obtained by following the guidelines here.

The following resources related to this article are available online at www.sciencemag.org (this infomation is current as of September 28, 2011):

Updated information and services, including high-resolution figures, can be found in the online version of this article at:
http://www.sciencemag.org/content/333/6050/1726.full.html

Supporting Online Material can be found at:
http://www.sciencemag.org/content/suppl/2011/09/21/333.6050.1726.DC1.html

A list of selected additional articles on the Science Web sites **related to this article** can be found at:
http://www.sciencemag.org/content/333/6050/1726.full.html#related

This article **cites 18 articles**, 7 of which can be accessed free:
http://www.sciencemag.org/content/333/6050/1726.full.html#ref-list-1

This article has been **cited by** 1 articles hosted by HighWire Press; see:
http://www.sciencemag.org/content/333/6050/1726.full.html#related-urls

This article appears in the following **subject collections:**
Materials Science
http://www.sciencemag.org/cgi/collection/mat_sci

Science (print ISSN 0036-8075; online ISSN 1095-9203) is published weekly, except the last week in December, by the American Association for the Advancement of Science, 1200 New York Avenue NW, Washington, DC 20005. Copyright 2011 by the American Association for the Advancement of Science; all rights reserved. The title *Science* is a registered trademark of AAAS.

and the "sharpness" of the Fano-like resonance, determined the observed beating behavior. This sensitivity of the model parameters for the two ROIs showed that the local response significantly varies on a 100-nm length scale, as was also seen for the coherence liftetime measured by 2D nanoscopy.

The hybridization of localized modes with long-lived dark modes and the associated appearance of long-lived localized electronic coherence are of general interest for surface-enhanced spectroscopy. Moreover, the coupled-oscillator model connects the observation of long-lived coherences in hot spot–related multiphoton photoemission on corrugated surfaces to the intensively studied phenomenon of electromagnetically induced transparency in plasmonic systems (*26*–*28*). The observation and investigation of such coupled modes had been restricted to ensembles of identical structures (*28*, *29*). With the application of 2D nanoscopy, we have resolved different Fano-like resonances within one individual hot-spot emission. Potential uses of 2D nanoscopy include polarization pulse shaping (*30*), which could allow mapping of the tensor character of the nonlinear response by selecting the appropriate polarization directions of the excitation subpulses. Indeed, the pulse shapes themselves could be varied, allowing the combination of 2D nanoscopy and coherent control techniques. Higher-order processes and systems with more than three levels could be investigated with pulse trains consisting of more than four pulses. Extension to short wavelengths (*12*) should also be possible.

References and Notes

1. J. Kasprzak *et al.*, *Nat. Photonics* **5**, 57 (2011).
2. D. Brinks *et al.*, *Nature* **465**, 905 (2010).
3. S. W. Hell, *Science* **316**, 1153 (2007).
4. L. Novotny, B. Hecht, *Principles of Nano-Optics* (Cambridge Univ. Press, Cambridge, 2006).
5. T. Guenther *et al.*, *Phys. Rev. Lett.* **89**, 057401 (2002).
6. S. Mukamel, *Principles of Nonlinear Optical Spectroscopy* (Oxford Univ. Press, New York, 1999).
7. S. Mukamel, *Annu. Rev. Phys. Chem.* **51**, 691 (2000).
8. D. M. Jonas, *Annu. Rev. Phys. Chem.* **54**, 425 (2003).
9. M. Cho, *Chem. Rev.* **108**, 1331 (2008).
10. P. Tian *et al.*, *Science* **300**, 1553 (2003).
11. P. F. Tekavec, G. A. Lott, A. H. Marcus, *J. Chem. Phys.* **127**, 214307 (2007).
12. S. Rahav, S. Mukamel, *Phys. Rev. A* **81**, 063810 (2010).
13. O. Schmidt *et al.*, *Appl. Phys. B* **74**, 223 (2002).
14. See supporting material on *Science* Online.
15. A. M. Weiner, *Rev. Sci. Instrum.* **71**, 1929 (2000).
16. S.-H. Shim, D. B. Strasfeld, Y. L. Ling, M. T. Zanni, *Proc. Natl. Acad. Sci. U.S.A.* **104**, 14197 (2007).
17. C. Timm, K. H. Bennemann, *J. Phys. Condens. Matter* **16**, 661 (2004).
18. W. A. Murray, W. L. Barnes, *Adv. Mater.* **19**, 3771 (2007).
19. N. Nilius, N. Ernst, H. Freund, *Phys. Rev. Lett.* **84**, 3994 (2000).
20. T. Hanke *et al.*, *Phys. Rev. Lett.* **103**, 257404 (2009).
21. M. Aeschlimann *et al.*, *J. Chem. Phys.* **102**, 8606 (1995).
22. R. C. Word *et al.*, *Appl. Phys. Lett.* **96**, 251110 (2010).
23. P. B. Johnson, R. W. Christy, *Phys. Rev. B* **6**, 4370 (1972).
24. H. Raether, in *Surface Plasmons on Smooth and Rough Surfaces and on Gratings*, G. Höhler, E. A. Niekisch, Eds. (Springer, Berlin, 1988), pp. 1–133.
25. E. Prodan *et al.*, *Science* **302**, 419 (2003).
26. S. Zhang *et al.*, *Phys. Rev. Lett.* **101**, 047401 (2008).
27. N. Liu *et al.*, *Nat. Mater.* **8**, 758 (2009).
28. B. Luk'yanchuk *et al.*, *Nat. Mater.* **9**, 707 (2010).
29. C. Ropers *et al.*, *Phys. Rev. Lett.* **94**, 113901 (2005).
30. T. Brixner, G. Gerber, *Opt. Lett.* **26**, 557 (2001).

Acknowledgments: All authors of this work are listed in alphabetical order. Supported by the Deutsche Forschungsgemeinschaft Priority Program "Ultrafast Nano-Optics" (SPP 1391). We thank B. Hecht for providing a nanostructured gold sample used for determining spatial resolution (*14*).

Supporting Online Material
www.sciencemag.org/cgi/content/full/science.1209206/DC1
Materials and Methods
Figs. S1 to S3
References (*31*–*39*)

1 June 2011; accepted 28 July 2011
Published online 11 August 2011;
10.1126/science.1209206

Geometry and Mechanics in the Opening of Chiral Seed Pods

Shahaf Armon,[1] Efi Efrati,[1] Raz Kupferman,[2] Eran Sharon[1]*

We studied the mechanical process of seed pods opening in *Bauhinia variegate* and found a chirality-creating mechanism, which turns an initially flat pod valve into a helix. We studied configurations of strips cut from pod valve tissue and from composite elastic materials that mimic its structure. The experiments reveal various helical configurations with sharp morphological transitions between them. Using the mathematical framework of "incompatible elasticity," we modeled the pod as a thin strip with a flat intrinsic metric and a saddle-like intrinsic curvature. Our theoretical analysis quantitatively predicts all observed configurations, thus linking the pod's microscopic structure and macroscopic conformation. We suggest that this type of incompatible strip is likely to play a role in the self-assembly of chiral macromolecules and could be used for the engineering of synthetic self-shaping devices.

Motion in plants is a highly nontrivial process. It is often based on anisotropic swelling and shrinkage, driven by the relatively slow variation of water content within the tissue (*1*). Swelling and shrinkage may lead to the accumulation of elastic energy and the buildup of stress. This stress can be released via mechanical instabilities, such as fracture, buckling, and snapping (*2*, *3*). The buildup of stress may also occur in sclerenchymal tissue (tissue made of dead cells) and is thus a process that can be analyzed from a purely mechanical point of view. Sclerenchymal tissue typically consists of fiber cells whose walls are made of layered cellulose fibrils with a preferred orientation. When absorbing/expelling water, the tissue expands/shrinks anisotropically, perpendicularly to the fibrils' orientation [(*1*), p. 200]. Changes in air humidity induce such uniaxial swelling/shrinkage that drive, for example, the opening and closure of a pine cone (*4*) and the penetration of wheat seeds into soil (*5*).

Chiral pod opening is a nontrivial example of hygroscopic (humidity-driven) motion in sclerenchymal tissue. In this process, two initially flat pod valves curl into helical strips of opposite handedness. A detailed study of the structure of pod valves in over 300 species of Leguminosae shows a wealth of architectures (*6*). We studied pod opening in *Bauhinia variegate* (Fig. 1, A and B), whose pod valves are known to consist of two fibrous layers, oriented roughly at ±45° with respect to the pod's longitudinal axis [supporting online material (SOM) text and fig. S1, x-ray scattering measurements and fig. S2]. It turns out that the mere presence of two layers that shrink in perpendicular directions is sufficient to drive the flat-to-helical transition in pod opening.

As a proof of concept, we constructed a mechanical analog of the Bauhinia pod that copies its geometry. We stretched two identical thin latex sheets uniaxially by the same elongation factor. We then glued one on top of the other in perpendicular directions (Fig. 1C). Once released from the external stretching, the composite object underwent the same shrinkage profile as the Bauhinia valve: The two layers shrunk uniaxially in perpendicular directions. Elongated strips cut out from the composite sheets were found to curl into helical configurations (Fig. 1F).

It is well known that uniaxial shrinkage of one layer in a bilayered sheet induces curvature, which accommodates the difference in length of the two layers. When the sheet is thin enough, it bends accordingly. Strips with a single intrinsic curvature have been studied extensively; large sheets adopt a cylindrical configuration, whereas narrow strips adopt helical configurations that are "cut from a cylinder" (*7*–*10*).

A qualitatively different situation occurs when two layers shrink perpendicularly. In such a case, the sheet "wants" to bend in two opposite and perpendicular directions—that is, they locally assume a saddle-like configuration (Fig. 1, D and E). This tendency to bend into a saddle creates a

---

[1] Racah Institute of Physics, Hebrew University of Jerusalem, Jerusalem 91904, Israel. [2] Institute of Mathematics, Hebrew University of Jerusalem, Jerusalem 91904, Israel.

*To whom correspondence should be addressed. E-mail: erans@vms.huji.ac.il

metric incompatibility: On the one hand, the in-plane rest lengths between surface elements require the surface to be metrically flat, to have zero Gaussian curvature. On the other hand, a saddle-like configuration has nonzero Gaussian curvature. Thus, the body cannot assume a stress-free configuration and must contain residual stress. The key feature of residually stressed bodies is that their configuration changes when they are dissected into smaller parts, reflecting the release of stored elastic energy.

Geometrically incompatible materials are well known in the mechanical literature and are described by the theory of "incompatible elasticity" (*11*, *12*). A mathematical theory for incompatible thin sheets was recently derived in (*13*, *14*). In this theory, thin sheets are modeled as two-dimensional surfaces. The configuration of a surface is fully characterized by two tensors: a metric tensor, a, which contains all information about lateral distances between points, and a curvature tensor, b, which contains information about the local curvature. An elastic sheet is characterized by two additional tensors that are intrinsic to its structure: a reference metric, $\overline{a}$, and a reference curvature, $\overline{b}$. These tensors represent the lateral distances and curvatures that would make the sheet locally stress-free. They are determined by the swelling/shrinkage distribution within the sheet. When $a \neq \overline{a}$, the sheet contains in-plane stretching deformations, and when $b \neq \overline{b}$, the sheet contains bending deformations. The total elastic energy is the sum of the stretching and bending energies,

$$E = E_s + E_B \sim$$

$$t\int\left[(1-\nu)|a-\overline{a}|^2 + \nu \mathrm{tr}^2(a-\overline{a})\right]dS +$$

$$t^3\int\left[(1-\nu)|b-\overline{b}|^2 + \nu \mathrm{tr}^2(b-\overline{b})\right]dS \quad (1)$$

where t is the thickness of the sheet, dS is the infinitesimal surface element, and ν is the Poisson ratio of the material. The ~ relation stands for proportionality, where the coefficients are constant material parameters. Given the material parameters $\overline{a}$ and $\overline{b}$, the system is postulated to minimize energy by choosing a configuration with optimal a and b.

Naïvely, one would think that the sheet can eradicate its elastic energy by settling on a configuration that satisfies $a = \overline{a}$ and $b = \overline{b}$. This, however, is not always possible: Every surface in space must fulfill a set of constraints—the Gauss-Codazzi-Mainardi equations—that connect between the metric and curvature tensors (*15*). If the local shrinkage is such that the resulting $\overline{a}$ and $\overline{b}$ do not satisfy these constraints, there cannot be any configuration in which $a = \overline{a}$ and $b = \overline{b}$ (SOM text). This is the mathematical formulation of the metric incompatibility discussed above. In such a case, the configuration of minimum energy is determined by a competition between the stretching and bending energies.

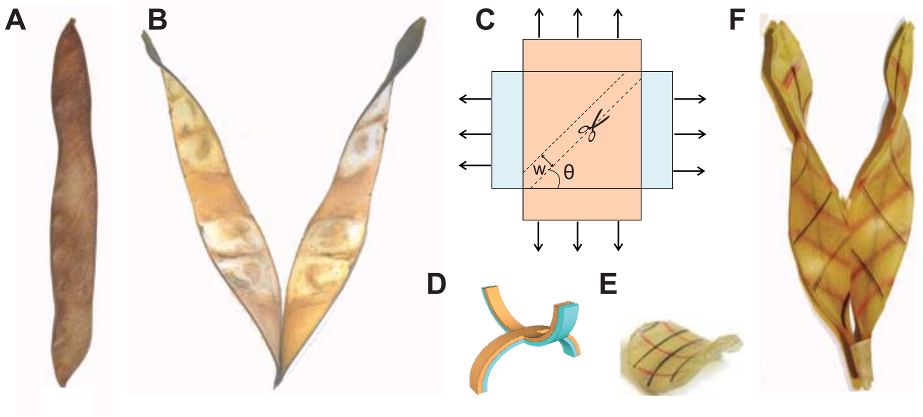

Fig. 1. (**A** and **B**) Closed and open Bauhinia pods. (**C**) Manufacturing of a mechanical analog. Two planar latex sheets are stretched uniaxially along perpendicular directions and then glued together, forming a residually stressed compound sheet. A strip is then cut from this sheet along a direction that forms an angle θ with one of the stretching directions. (**D**) Illustration of the target curvatures induced by the stretching profile. (**E**) Equilibrium configuration of a small circle cut from the stretched bilayer. The perpendicular lines represent the stretching directions. (**F**) Pod-like configurations mimicked by two narrow strips cut from the latex sheets at angles θ = 45°,135° (the grids are parallel to the directions of principal curvature).

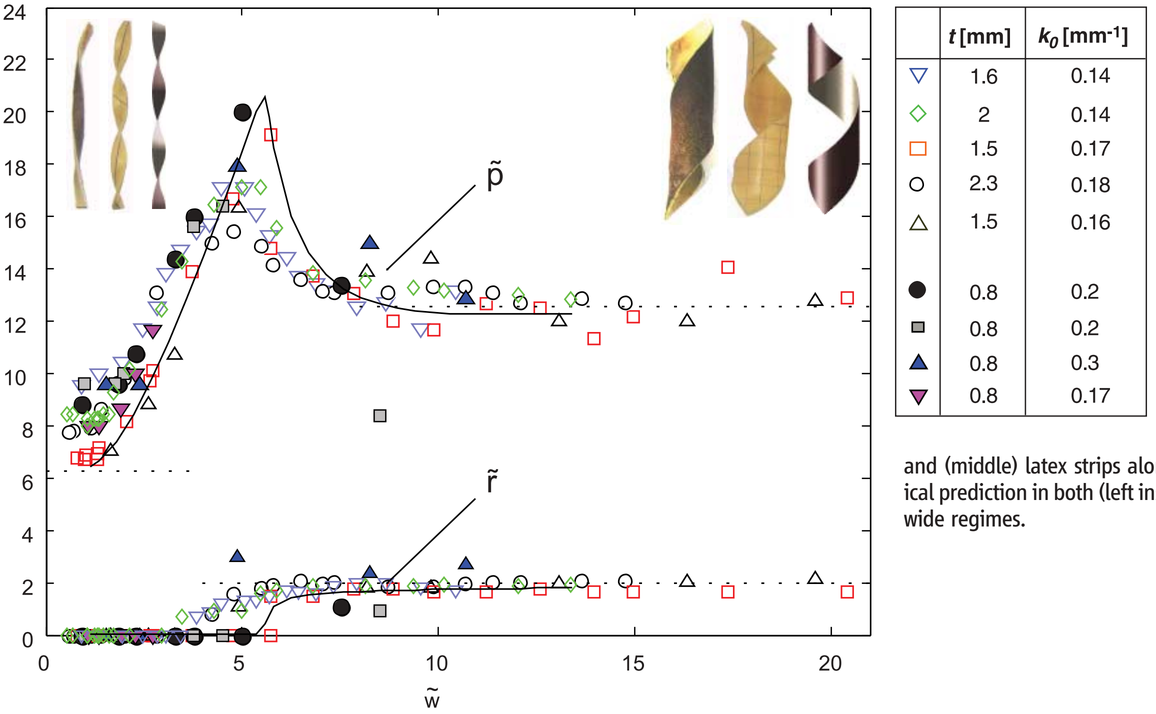

	t [mm]	k_0 [mm^{-1}]
▽	1.6	0.14
◇	2	0.14
□	1.5	0.17
○	2.3	0.18
△	1.5	0.16
●	0.8	0.2
■	0.8	0.2
▲	0.8	0.3
▼	0.8	0.17

Fig. 2. Dimensionless radius, $\tilde{r} = r\kappa_0$, and pitch, $\tilde{p} = p\kappa_0$, versus dimensionless width, $\tilde{w} = w\sqrt{\kappa_0 t}$, for various strips cut from latex sheets at θ = 45° (open symbols) and Bauhinia pods (solid symbols); different samples differ in κ_0 and t (legend to right). The solid lines are the theoretical predictions, and the dotted lines are the asymptotic limiting values (Eqs. 4 and 5). Both insets show equilibrium configurations of (left) Bauhinia and (middle) latex strips along with (right) the theoretical prediction in both (left inset) narrow and (right inset) wide regimes.

The first step in modeling the shaping of Bauhinia pods (or the mechanical model) is to determine the reference tensors $\bar{a}$ and $\bar{b}$. Each of the fibrous layers that construct the valve is separately planar. This implies that the reference metric is Euclidean and can be written in the form

$$\bar{a} = \begin{pmatrix} 1 & 0 \\ 0 & 1 \end{pmatrix} \qquad (2)$$

Measurements on segments of Bauhinia pods cut along the two directions of principal curvature exhibit oppositely curved arcs of approximately the same radius. This validates our assertion that $\bar{b}$ exhibits at each point two principal curvatures of the same magnitude but of opposite signs. Adopting coordinates (x, y) that are parallel to the directions of principal curvature, we obtain a saddle-like (hyperbolic) reference curvature tensor of the form

$$\bar{b} = \begin{pmatrix} \kappa_0 & 0 \\ 0 & -\kappa_0 \end{pmatrix} \qquad (3)$$

where κ_0 is the magnitude of the reference curvature. In Bauhinia pods, the directions of principal curvature form an angle of 45° with respect to the longitudinal axis. In strips cut out from latex sheets, this angle can be determined at will. A strip is characterized by the following parameters: a thickness t, a width w, a length L, an induced curvature κ_0, and an angle θ between the strip's longitudinal axis and a direction of principal curvature.

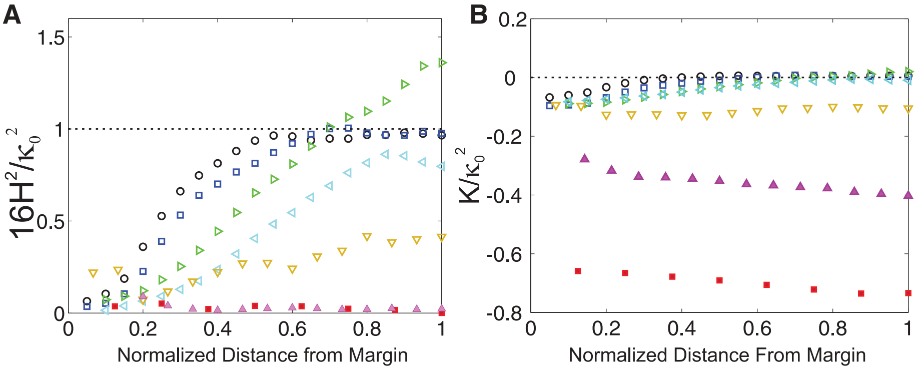

Fig. 3. Surface morphology of latex sheets cut at 45°. (**A**) Normalized mean curvature squared, $16H^2/\kappa_0^2$, and (**B**) normalized Gaussian curvature, K/κ_0^2, both as function of the distance (in units of half width) from the edge. The thickness of the sheet is 1.5 mm. The different symbols correspond to strips of widths 5, 8, 18, 25, 30, 40, and 60 mm [bottom to top in (B)].

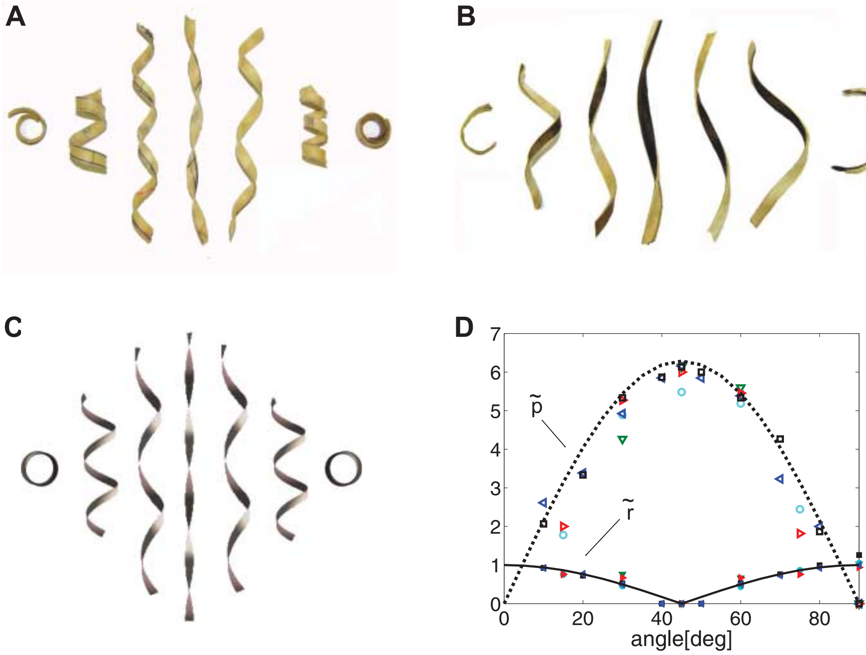

Fig. 4. Configurations of narrow strips cut at angles 0°, 15°, 30°, 45°, 60°, 75°, and 90° from (**A**) a latex sheet and (**B**) Bauhinia pods. (**C**) Theoretically predicted configurations. (**D**) Dependence of radius and pitch on angle. Symbols correspond to latex sheets, whereas the lines are the theoretical predictions.

A quantitative study of strips cut out from Bauhinia pods and from latex sheets at an angle of $\theta = 45°$ exhibits two different regimes: Wide strips adopt a configuration close to a cut from a cylindrical envelope ("cylindrical helices"), whereas narrow strips exhibit a "pure twist," where the strip's centerline is straight ("twisted helices"). At the coarsest level, we may characterize the shape of the strips by two parameters: the radius r and the pitch p of the strip's midcurve. Figure 2 shows results for a collection of strips cut from both Bauhinia pods and latex sheets. For each sample, we measured the parameters t, w, r, p, and κ_0 (κ_0 was estimated by measuring the curvature of very thin strips cut along principal directions). We plotted a dimensionless pitch $\tilde{p} = p\kappa_0$ and a dimensionless radius $\tilde{r} = r\kappa_0$ as functions of a dimensionless width $\tilde{w} = w\sqrt{\kappa_0/t}$. With this scaling, both pod tissue and latex data were found to collapse to a single functional behavior. We found a critical transition between the two regimes. For $\tilde{w} < w_{\mathrm{crit}} \approx 2.5$, the radius $\tilde{r}$ is nearly 0, exhibiting a forward bifurcation at the critical value. The pitch $\tilde{p}$ attains a maximum at a value of $\tilde{w}$ of about $\tilde{w}_{\mathrm{crit}}$.

The theoretical study consists of minimizing the energy (Eq. 1) of a strip with reference tensors $\bar{a}$ and $\bar{b}$ as given by (Eq. 2) and (Eq. 3). Dimensional analysis indicates that the stretching energy scales like $tw(\kappa_0 w)^4$, whereas the bending energy scales like $t^3 w\kappa_0^2$. Thus, one expects the occurrence of a stretching-dominated regime for large w and a bending-dominated regime for small w. The transition between the two regimes is expected to occur when the two energies are of comparable magnitude, when $w = \sqrt{t/\kappa_0}$, or $\tilde{w} \approx 1$.

When $\tilde{w} \gg 1$, the stretching term dominates, and $a \approx \bar{a} = I$, except within a bending-dominated boundary layer of characteristic width $\sqrt{t/\kappa_0}$. Thus, b aims to optimally approximate $\bar{b}$, under the constraints that the metric be Euclidean. At equilibrium, one of the principal curvatures is found to coincide with the reference curvature (up to a multiplicative factor depending on the Poisson ratio ν), whereas the second principal curvature is 0,

$$b = (1-\nu)\begin{pmatrix} \kappa_0 & 0 \\ 0 & 0 \end{pmatrix} \text{ or } b = (1-\nu)\begin{pmatrix} 0 & 0 \\ 0 & -\kappa_0 \end{pmatrix}.$$

The two solutions are equally stable. The configuration looks like strips cut out from the envelope of a cylinder, with a centerline that is a helix of radius and pitch (Fig. 2, right inset):

$$r = \frac{p}{2\pi} = \frac{1}{(1-\nu)\kappa_0} \qquad (4)$$

Such cylindrical helices are similar to configurations observed in strips with a single intrinsic curvature (*7–10*). Yet, there is a fundamental difference between the two cases because in the case of a single curvature, $\bar{a}$ and $\bar{b}$ are compatible, and there is no mechanical frustration. In the presently studied case, $\bar{a}$ and $\bar{b}$ are incompatible, resulting in stored mechanical energy. Two manifestations of this geometric frustration are the bistability of the equilibrium and the configurational change occurring when the strip is dissected.

When $\tilde{w} \ll 1$ (narrow strips), the equilibrium configuration is bending-dominated, $b \approx \bar{b}$. Now, it is the metric a that best approximates (in a mean square sense) the reference metric $\bar{a}$, among all metrics compatible with $\bar{b}$. It can be shown that at equilibrium, $a \approx \bar{a}$ in the vicinity of the mid-curve, which is all that is needed for predicting the shape of the mid-curve.

The configurations in the narrow regime are twisted helices and are similar to configurations found in (stretch-free) liquid membranes (*16*, *17*). Once again, there is a fundamental difference between the two cases because twisted helices in liquid membranes are stress-free. In the present study, they result from a compromise between stretching and bending energies.

The radius and pitch in the narrow regime are

$$r = 0 \text{ and } p = \frac{2\pi}{\kappa_0} \qquad (5)$$

The limiting values (Eq. 4) and (Eq. 5) are represented in Fig. 2 as dotted lines and are found to agree with measured data. Lastly, in the intermediate regime both stretching and bending are comparably important, and one has to minimize the total energy with respect to both a and b. The calculation of a global minimizer can be done numerically, as described in the SOM text. The predicted dimensionless radius and pitch are displayed as functions of $\tilde{w}$ in Fig. 2B (solid line) and show good agreement with experimental data.

The transition between the two limiting regimes—wide versus narrow strips—is also manifested in the geometry of the surface. One way to characterize a surface is via the local values of its mean curvature, H, and Gaussian curvature, K, which are the respective mean and product of the two principal curvatures. In Fig. 3, we plot H^2 and K as function of the distance from the edge for a collection of latex strips differing only in width. These data were extracted by measuring the surface topography of the latex strips with optical profilometry. Each scan provides us with a map of the surface height, from which we computed the local values of H and K by discrete differentiation. We then averaged H and K over points that are at equal distance from the edge of the strip. Narrow strips, $\tilde{w} \le \tilde{w}_{\text{crit}}$, are approximately minimal surfaces with mean curvatures of uniformly 0 as dictated by $\bar{b}$. Above the critical width, H is no longer uniformly 0. For wide strips, H reaches the predicted value of $(1 - \nu)\kappa_0$ far enough from the edge (dotted line) while remaining 0 at the edge, with a boundary layer connecting the two regions (*14*). For wide strips, $K \approx 0$ as determined by (the Euclidean) $\bar{a}$, whereas for narrow ones, K tends toward the asymptotic value of $-\kappa_0^2$ (–1 in the units used in the plot) as $w \rightarrow 0$. Thus, our model is capable of predicting not only the global shape of the helical strips but their surface topography as well.

A natural question is whether the transition between the narrow and wide regimes is continuous or not; more precisely, is the change in equilibrium configuration continuous as $\tilde{w}$ crosses the critical value of $\tilde{w}_{\text{crit}}$? Both our calculations and measurements indicate that the transition is continuous, although sharp. For example, Fig. 3A shows that as $\tilde{w}$ approaches from above the value of $\tilde{w}_{\text{crit}}$, the mean curvature tends continuously to zero.

Our theoretical and mechanical models capture well the behavior of Bauhinia valves and link quantitatively between the microscopic structure and the macroscopic configurations. Yet, they have an even wider scope of applicability. We next studied the dependence of the equilibrium configuration on the angle θ. Configurations of latex, Bauhinia, and theoretically predicted strips, respectively, are shown in Fig. 4, A to C, for fixed width and varying θ. The dependence of the radius and the pitch on the angle for latex strips are shown in Fig. 4D. The parameters correspond to the "narrow" regime, $\tilde{w} < \tilde{w}_{\text{crit}}$. For θ = 0° and θ = 90°, the strips' longitudinal axis coincides with a direction of principal curvature. As a result, the shapes are circular, with curvature approximately equal to the corresponding principal curvature. As θ is increased from 0° to 45°, the pitch increases, and the radius decreases, until a pure twist is obtained at 45°. The same behavior is obtained when the angle decreases from 90° to 45°. The handedness of the configurations is reversed for strips cut at angles between 90° and 180° (not shown). This demonstrates that the handedness of the helices is not a bulk material property but rather depends on the global geometry of the sample.

We have also conducted an experimental study of the dependence of the equilibrium configuration on the angle θ in the "wide" regime, $\tilde{w} < \tilde{w}_{\text{crit}}$ (data not shown). In this regime, two bistable configurations emerge, each being flat along another direction of principal curvature. Both states have the same handedness and the same bulk energy density, so that the globally stable state is determined by boundary effects. The two metastable states are indistinguishable at θ = 45°. For θ = 0°,90°, the two bistable states correspond to the two states of tape springs, which were studied in (*18*), for an example.

The only inputs in our model are $\bar{a}$ and $\bar{b}$ and not any specific swelling/shrinkage profiles. Many different combinations of anisotropic layered growth would lead to the same intrinsic geometry—the same $\bar{a}$ and $\bar{b}$. For example, the same form of $\bar{b}$ is achieved if the angle between the swelling/shrinkage directions is not 90° or even under isotropic growth of one layer together with an anisotropic growth of the other (SOM text and figs. S3 and S4). Thus, the mechanism we have presented is quite general and is expected to manifest in different systems with different internal structures, consistently with the diverse valve architectures reported in (*6*).

The present study is potentially applicable to systems of different scales and contexts. For example, many organic and inorganic macromolecules are found in different helical configurations (*9*, *16*, *17*, *19*). In our model, the only nontrivial property of the sheet is its saddle-like reference curvature tensor. It can therefore be relevant to any sheet with such spontaneous curvatures, including monolayers and sheets with different microstructures. Macromolecules made of chiral molecules are often modeled by introducing a term in the bending energy that accounts for a spontaneous twist. It can be shown that geometrically, a sheet with a spontaneous twist is equivalent to one with hyperbolic reference curvature tensor (SOM text). Indeed, a transition qualitatively similar to the one presented in Fig. 2 was predicted in (*20*, *21*). After translating the parameters of (*21*), we found their predicted value for $\tilde{w}_{\text{crit}}$ to be similar to ours. It would be interesting to see whether our model, which accounts for a wider range of intrinsic geometries, could describe configurations of macromolecules that are currently not well understood (*19*). Lastly, mechanisms such as the one studied here can be implemented by using inducible responsive materials. Such bio-mimicking designs have an applicative potential as soft actuators (for a proof of concept, see movies S1 and S2).

References and Notes

1. A. Fahn, E. Werker, in *Seed Biology*, T. T. Kozlowski, Ed. (Academic Press, New York, 1972), pp. 151–221.
2. J. M. Skotheim, L. Mahadevan, *Science* **308**, 1308 (2005).
3. Y. Forterre, J. M. Skotheim, J. Dumais, L. Mahadevan, *Nature* **433**, 421 (2005).
4. E. Reyssat, L. Mahadevan, *J. R. Soc. Interface* **6**, 951 (2009).
5. R. Elbaum, L. Zaltzman, I. Burgert, P. Fratzl, *Science* **316**, 884 (2007).
6. A. Fahn, M. Zohary, *Phytomorphology* **5**, 99 (1955).
7. X. Y. Kong, Y. Ding, R. Yang, Z. L. Wang, *Science* **303**, 1348 (2004).
8. L. Zhang, E. Deckhardt, A. Weber, C. Schonenberger, D. Grutzmacher, *Nanotechnology* **16**, 655 (2005).
9. P. X. Gao *et al.*, *Science* **309**, 1700 (2005).
10. E. Reyssat, L. Mahadevan, *Europhys. Lett.* **93**, 54001 (2011).
11. C.-C. Wang, *Arch. Ration. Mech. Anal.* **27**, 33 (1967).
12. E. Kroner, in *Les Houches Summer School Proceedings*, R. Balian, M. Kleman, J.-P. Poirier, Eds. (North-Holland, Amsterdam, 1981), pp. 282–315.
13. E. Efrati, E. Sharon, R. Kupferman, *J. Mech. Phys. Solids* **57**, 762 (2009).
14. E. Efrati, E. Sharon, R. Kupferman, *Phys. Rev. E Stat. Nonlin. Soft Matter Phys.* **80**, 016602 (2009).
15. D. J. Struik, *Lectures on Classical Differential Geometry* (Dover, New York, ed. 2, 1961).
16. R. Oda, I. Huc, M. Schmutz, S. J. Candau, F. C. MacKintosh, *Nature* **399**, 566 (1999).
17. J. V. Selinger, M. S. Spector, J. M. Schnur, *J. Phys. Chem. B* **105**, 7157 (2001).
18. K. A. Seffen, S. Pellegrino, *Proc. R. Soc. Lond. A* **455**, 1003 (1999).
19. Y. V. Zastavker *et al.*, *Proc. Natl. Acad. Sci. U.S.A.* **96**, 7883 (1999).
20. R. L. B. Selinger, J. V. Selinger, A. P. Malanoski, J. M. Schnur, *Phys. Rev. Lett.* **93**, 158103 (2004).

21. R. Ghafouri, R. Bruinsma, *Phys. Rev. Lett.* **94**, 138101 (2005).

Acknowledgments: We are grateful to Y. Abraham and U. Raviv for performing the small-angle x-ray scattering measurements. R.K. was partially supported by the Israeli Science Foundation. E.S. was partially supported by the European Research Council SoftGrowth project. S.A. was supported by the Eshkol Scholarship sponsored by the Israeli Ministry of Science.

Supporting Online Material
www.sciencemag.org/cgi/content/full/333/6050/1726/DC1
SOM Text
Figs. S1 to S4
References
Movies S1 and S2

7 February 2011; accepted 27 July 2011
10.1126/science.1203874

The Role of a Bilayer Interfacial Phase on Liquid Metal Embrittlement

Jian Luo,[1]* Huikai Cheng,[2] Kaveh Meshinchi Asl,[1] Christopher J. Kiely,[2] Martin P. Harmer[2]*

Intrinsically ductile metals are prone to catastrophic failure when exposed to certain liquid metals, but the atomic-level mechanism for this effect is not fully understood. We characterized a model system, a nickel sample infused with bismuth atoms, by using aberration-corrected scanning transmission electron microscopy and observed a bilayer interfacial phase that is the underlying cause of embrittlement. This finding provides a new perspective for understanding the atomic-scale embrittlement mechanism and for developing strategies to control the practically important liquid metal embrittlement and the more general grain boundary embrittlement phenomena in alloys. This study further demonstrates that adsorption can induce a coupled grain boundary structural and chemical phase transition that causes drastic changes in properties.

In liquid metal embrittlement (LME), intrinsically ductile metals, such as Al, Cu, and Ni, are prone to catastrophic brittle intergranular fracture at unusually low stress levels when exposed to certain liquid metals (*1*). LME can cause cracking during and/or after hot dip galvanizing or welding of steels and other nonferrous structural alloys. Furthermore, understanding LME is important for enabling the usage of liquid metals in the next generation of nuclear power generation systems and novel spallation target systems for nuclear waste incineration. In LME, the failure is known to originate at the grain boundaries (GBs), where the adsorption of the liquid metal element occurs (*2*–*4*), but an exact understanding of the embrittlement mechanism at an atomic level has puzzled the materials and physics communities for over a century. We have characterized GBs in a model LME system, Ni-Bi, by using aberration-corrected high-angle annular dark-field (HAADF) scanning transmission electron microscopy (STEM). Our study suggests that the embrittlement in Ni-Bi is due to bilayer adsorption of Bi atoms at general (i.e., high-energy and low-symmetry) GBs.

In a broader context, observation of these bilayers in a simple metallic system (Ni-Bi) fills a knowledge gap to demonstrate the general existence of discrete nanoscale GB-stabilized phases (also called complexions; see Fig. 1) (*5*). Whereas the existence of surface phases is well established (*6*), the identification of GB analogs at internal interfaces offers a different perspective for solving a variety of outstanding scientific problems (*7*, *8*). The coexistence of multiple interfacial phases at GBs with markedly different

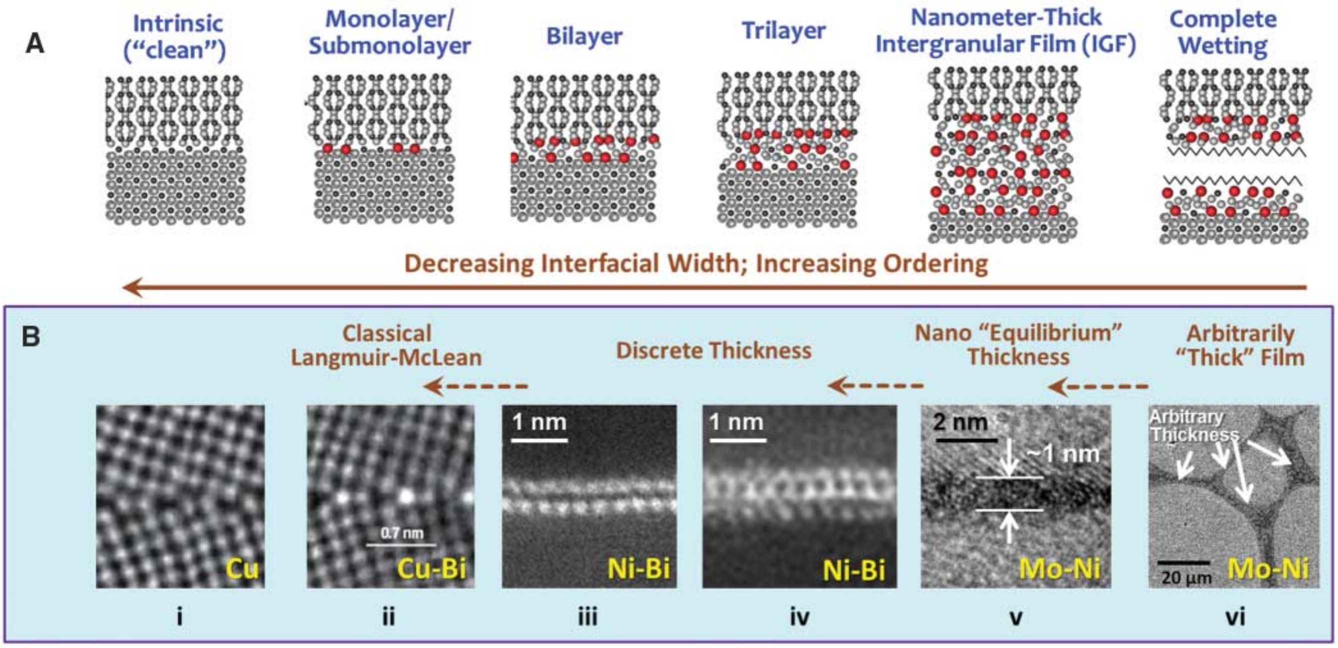

Fig. 1. (**A**) Six distinct interfacial phases have been observed in alumina and termed GB complexions (*7*, *8*). These schematics are adapted from (*7*) with permission. (**B**) Analogous interfacial phases in metals. The direct STEM HAADF observation of the most controversial bilayer and trilayer interfacial phases in a simple metal system, Ni-Bi, where the interpretation of images and their thermodynamic origin are less equivocal, authenticates the existence and generality of this series of generic interfacial phases. The physical origins of the nanoscale interfacial phases that are intermediate to the classical L-M adsorption and complete GB wetting are illustrated and discussed in the text. Micrographs i and ii are adapted from (*28*), and micrographs v and vi are adapted from (*11*) with permissions. Micrographs iii and iv are from the current work.

---

[1] School of Materials Science and Engineering, Center for Optical Materials Science and Engineering Technology, Clemson University, Clemson, SC 20634, USA. [2] Department of Materials Science and Engineering, Center for Advanced Materials and Nanotechnology, Lehigh University, Bethlehem, PA 18015, USA.

*To whom correspondence should be addressed. E-mail: mph2@lehigh.edu (M.P.H.); jluo@alum.mit.edu (J.L.)